

# Test-Time Conditioning with Representation-Aligned Visual Features

Nicolas Sereyjol-Garros<sup>1</sup> Ellington Kirby<sup>1</sup> Victor Letzelter<sup>1,2</sup> Victor Besnier<sup>1</sup> Nermin Samet<sup>1</sup>

## Abstract

While representation alignment with self-supervised models has been shown to improve diffusion model training, its potential for enhancing inference-time conditioning remains largely unexplored. We introduce Representation-Aligned Guidance (REPA-G), a framework that leverages these aligned representations, with rich semantic properties, to enable test-time conditioning from features in generation. By optimizing a similarity objective (the *potential*) at inference, we steer the denoising process toward a conditioned representation extracted from a pre-trained feature extractor. Our method provides versatile control at multiple scales, ranging from fine-grained texture matching via single patches to broad semantic guidance using global image feature tokens. We further extend this to multi-concept composition, allowing for the faithful combination of distinct concepts. REPA-G operates entirely at inference time, offering a flexible and precise alternative to often ambiguous text prompts or coarse class labels. We theoretically justify how this guidance enables sampling from the potential-induced tilted distribution. Quantitative results on ImageNet and COCO demonstrate that our approach achieves high-quality, diverse generations. Code is available at <https://github.com/valeoai/REPA-G>.

## 1. Introduction

In recent years, generative models have achieved impressive results in image synthesis (Labs, 2024; Esser et al., 2024), reaching near photo-realistic quality. This progress has been driven in particular by diffusion models (Song et al., 2021b; Ho et al., 2020) and flow matching (Lipman et al., 2023; Ma et al., 2024) approaches, which iteratively

<sup>1</sup>Valeo.ai, Paris, France <sup>2</sup>LTCl, Télécom Paris, Institut Polytechnique de Paris, France. Correspondence to: Nicolas Sereyjol-Garros <nicolas.sereyjol-garros@valeo.com>.

Preprint. February 4, 2026.

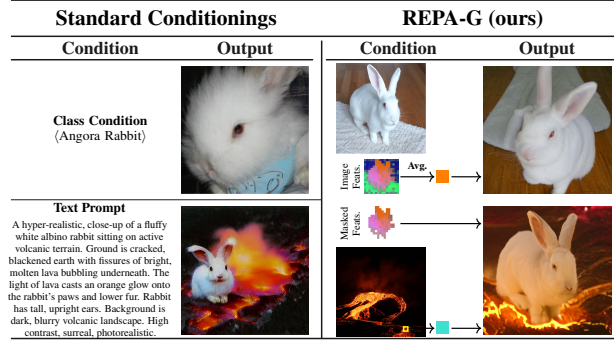


**Figure 1. Comparing class-label, text-prompt, and REPA-G conditioning.** All models are trained on ImageNet. (*Top*) We average extracted features (■) from an anchor image to generate a generic “rabbit” image. (*Bottom*) We combine a masked feature map with a specific “lava” patch (■) to synthesize a rabbit on a volcano. While text prompts require lengthy descriptions and often lack precision, our feature-based conditioning offers better compositional control and provides more precise generation.

remove Gaussian noise from images during generation. Recently, a line of work has shown that, beyond the standard denoising objective, diffusion models can be trained to align their intermediate representations (Wang et al., 2025; Leng et al., 2025; Tian et al., 2025; Sereyjol-Garros et al., 2026) using pre-trained self-supervised learning models such as DINOv2 (Oquab et al., 2024). This representation alignment has been shown to accelerate training and improve sample quality. However, it remains unclear how these aligned representations can be effectively leveraged at inference time.

Beyond improving sample quality, controllability has emerged as a central challenge in image synthesis. Current conditioning strategies typically rely on class labels (Peebles & Xie, 2023) or textual descriptions (Rombach et al., 2022). Class-based conditioning provides only coarse control and is limited to predefined categories. Using text is more flexible but often imprecise and ambiguous (see Figure 1).

In this work, we leverage representation alignment training in diffusion models for conditional image generation. Our method (REPA-G) enables test-time visual conditioning via inference-time optimization by exploiting the alignment between a diffusion model’s internal representations and those of a pre-trained self-supervised model. By steering the

diffusion process toward target feature tokens, we achieve fine-grained control over generation without relying on a fixed set of class labels or potentially ambiguous textual prompts. This improves controllability while preserving flexibility and generality.

Specifically, we extract visual tokens from a real image using the same self-supervised learning network used during representation alignment training, for example DI-NOv2 (Oquab et al., 2024). We then guide generation using a single token or a set of tokens that capture the concept at varying levels of granularity. The model can be conditioned with multiple tokens extracted from a mask to preserve shape or pose. Finally, conditioning with the average of all image tokens provides a broad concept signal such as *rabbit, car* (see Figure 1).

We achieve this by computing the gradient of a *potential* that quantifies the alignment between representations of generated sample and conditioning data points, corresponding to semantic *concepts* tokens. In addition to predicted scores and the velocities, the sampling procedure is guided by this gradient, to the aim of ultimately sampling from a tilted distribution induced by the defined potential. We then generalize the idea to multiple potentials by aligning with several concept tokens simultaneously. Our proposed method pulls relevant features toward the specified concepts enabling faithful generation, and makes it possible to generate flexible compositions (see Figure 1).

In summary, we introduce the first test-time visual conditioning framework for diffusion models trained with representation alignment. Our contributions are as follows:

**We introduce Representation-Aligned Guidance (REPA-G).** REPA-G leverages representation alignment during sampling to align internal diffusion features with targets from a self-supervised encoder.

**We analyze the properties of the representation space for feature conditioning.** We justify that (i) this guidance enables sampling from the steered density and (ii) that self-supervised features are well suited for this task.

**We conduct extensive experiments, showing control over concrete and abstract visual concepts.** Our framework handles objects, textures, and background semantics, enabling both spatial and concept-level guidance as well as concept composition. Our method operates entirely at inference time without requiring fine-tuning nor retraining.

## 2. Related Works

**Representation Alignment for Generation.** Image synthesis is dominated by diffusion and flow matching models (Ho et al., 2020; Lipman et al., 2023). These methods enable photorealistic image generation at the cost of

a slow generation speed and a long training time (Song et al., 2021a). Recently, REPA (Yu et al., 2025) argues that the training speed of latent diffusion models is largely constrained by how quickly they learn a meaningful internal image representation (Wang et al., 2025). To mitigate this, they guide the learning by aligning intermediate model projections with feature maps from a pre-trained encoder, which accelerates training and improves generation quality. iREPA (Singh et al., 2025) shows that spatial structure in representations correlates more strongly with generation quality than global information. They use a convolutional projection instead of a MLP and a spatial normalization layer. VA-VAE (Yao et al., 2025) applies a latent alignment loss solely in the VAE latent space prior to diffusion training. Finally, REPA-E (Leng et al., 2025) enables end-to-end training by backpropagating the REPA loss through both the diffusion model and the VAE encoder. This jointly shapes their internal representations, yielding better alignment and higher-quality generations.

**Conditional Generation in Diffusion Models.** Beyond sample quality, recent research has increasingly emphasized controllability as a central aspect of image synthesis, often considered as important as visual fidelity or diversity (Hertz et al., 2023; Couairon et al., 2023). Early adaptations of diffusion models to image generation were largely unconditional (Ho et al., 2020). Subsequent works introduced conditioning through auxiliary classifiers (Dhariwal & Nichol, 2021) or classifier-free guidance (Ho & Salimans, 2022). Today, diffusion models are commonly conditioned during training on various modalities, including class labels (Dhariwal & Nichol, 2021), textual descriptions (Rombach et al., 2022; Saharia et al., 2022), or reference images for image editing (Labs et al., 2025). These mechanisms typically require task-specific training and architectural modifications that remain fixed at inference. An alternative line of work explores post-training strategies (Zhang et al., 2023; Ye et al., 2023; Stracke et al., 2024), which enable conditioning on structural signals like depth or edge maps. While effective, these approaches introduce additional parameters and require extra post-training steps, increasing both model complexity and computational cost.

Our method enables test-time control in unconditionally trained flow models, without additional training or parameters, provided that representation alignment holds. This is orthogonal to image inpainting methods (Xie et al., 2023; Yang et al., 2023), which typically require explicit training on masked data and text prompts, often using Stable Diffusion models (Rombach et al., 2022) pre-trained on large-scale, scene-centric datasets. In contrast, REPA-G targets general guidance in generation, allowing conditioning on arbitrary features rather than text.

To the best of our knowledge, we are the first to explore such

test-time conditioning in this context, as existing literature on training-free guidance remains sparse. Kadkhodaie et al. (2025) study the interpretability of intermediate features in an unconditional diffusion model, rather than proposing a test-time conditioning method. Using an unconditional UNet trained on ImageNet, they probe what internal channels encode during denoising by constraining sampling to match an activation summary extracted from a reference image, then observing which attributes stay invariant. In contrast, we make test-time conditioning the core goal and evaluate it quantitatively and qualitatively.

### 3. Preliminaries

Let  $p_0$  be a (clean) data distribution on  $\mathcal{X}$ , which may correspond to pixel space in image generation. We describe hereafter the training of a flow matching model to be able to produce new samples from  $p_0$  while being “representation-aligned” with a pretrained backbone  $\phi$ .

**Flow Models.** Let  $p_1 = \mathcal{N}(0, I)$  be a standard Gaussian prior on  $\mathcal{X}$ . We define an interpolation process by sampling independently  $x_0 \sim p_0$  and  $x_1 \sim p_1$  and set  $x_t = \alpha_t x_0 + \sigma_t x_1$ , with typically  $\alpha_t = 1 - t$  and  $\sigma_t = t$ . For such a process, there exists a *probability-flow* ordinary differential equation (PF-ODE)  $\dot{x} = v^*(x, t)$  with a velocity field  $v^*(x, t)$  such that the probability flow  $p_t$  induced by the PF-ODE at time  $t$  is the time-marginal density of  $x_t$ . Conditional flow models train a velocity field  $v_\theta : (x, t) \in \mathcal{X} \times [0, 1] \rightarrow v_\theta(x, t) \in \mathcal{X}$  with

$$\mathcal{L}^{\text{diff}}(\theta) = \mathbb{E}_{t \sim \mathcal{U}(0,1), (x_0, x_1) \sim p_0 \times p_1} \left[ \|v_\theta(x_t, t) - \dot{x}_t\|_2^2 \right]. \quad (1)$$

A necessary condition for  $\mathcal{L}^{\text{diff}}$  to reach a global optimum at  $\theta = \theta^*$  is that, for each  $x$  and  $t$ , we get:

$$v_\theta(x, t) = v^*(x, t) = \mathbb{E}_{(x_0, x_1) \sim p_0 \times p_1} [\dot{x}_t \mid x_t = x]. \quad (2)$$

Using Tweedie’s formula (Efron, 2011), we can relate  $v^*$  to the score  $\nabla_x \log p_t(x)$  of the marginal distribution  $p_t$  of  $x_t$ . In the particular case of  $(\alpha_t, \sigma_t) = (1 - t, t)$ , we have:

$$v^*(x, t) = -\frac{1}{1-t}x - \frac{t}{1-t}\nabla_x \log p_t(x). \quad (3)$$

To sample from  $p_0$ , one can draw  $x_1 \sim p_1$  and integrate the PF-ODE backward from  $t = 1$  to  $t = 0$  using, e.g., Euler’s method. In practice, a Stochastic Sampler (e.g., Euler-Maruyama) can be used to improve sample quality during inference as in Yu et al. (2025), integrating a reverse-time stochastic differential equation (SDE) of the form

$$dx_t = (v^*(x_t, t) - t\nabla_x \log p_t(x_t)) dt + \sqrt{2t}d\bar{W}_t, \quad (4)$$

which shares the same marginals  $p_t$  as the PF-ODE. The term in parentheses corresponds to the *drift*, while the

stochastic term  $\sqrt{2t}d\bar{W}_t$  is the *diffusion*, where  $\bar{W}_t = W_{1-t}$  denotes a (time-reversed) standard Brownian motion. In (4),  $v^*$  is replaced by  $v_\theta$  and the estimated score  $\nabla_x \log p_t(x)$  is deduced from (3), where  $t$  is clipped to  $\varepsilon > 0$  to avoid instabilities. Unless otherwise stated, we use the SDE sampling strategy through (4) hereafter.

**Representation Alignment.** The flow model  $v_\theta$  can be expressed as  $v_\theta = g_\theta \circ f_\theta$  where  $f_\theta : \mathcal{X} \times [0, 1] \rightarrow \mathcal{Z}$ , projects input into a latent representation  $f_\theta(x_t, t)$  at a given layer, and  $g_\theta : \mathcal{Z} \rightarrow \mathcal{X}$  process this representation to construct the prediction. REPA (Yu et al., 2025) suggests optimizing (1) along with an alignment loss using an additional projection layer  $h_\theta : \mathcal{Z} \rightarrow \mathcal{Z}'$ :

$$\mathcal{L}^{\text{align}}(\theta) = -\mathbb{E}_{\substack{t \sim \mathcal{U}(0,1) \\ (x_0, x_1) \sim p_0 \times p_1}} \left[ \mathcal{V}((h_\theta \circ f_\theta)(x_t, t), \phi(x_0)) \right]. \quad (5)$$

in a compound loss  $\mathcal{L}^{\text{diff}}(\theta) + \beta\mathcal{L}^{\text{align}}(\theta)$ , with  $\beta > 0$ .

In (5),  $\mathcal{V} : \mathcal{Z}' \times \mathcal{Z}' \rightarrow \mathbb{R}$  is a *potential* that measures similarity between the features, predicted by  $f_\theta$  and projected with  $h_\theta$ , with those of a pretrained (frozen) backbone  $\phi : \mathcal{X} \rightarrow \mathcal{Z}'$  evaluated on the *clean* image. When  $\mathcal{Z}' = \mathbb{R}^{N \times d}$ ,  $N$  is the number of features and  $d$  is the features dimension,  $\mathcal{V}$  is typically expressed as an average patch-wise similarity  $\mathcal{V}(h_t, h^*) = \frac{1}{N} \sum_{n=1}^N \langle [h_t]_n, [h^*]_n \rangle$  where  $\langle \cdot, \cdot \rangle$  denotes the euclidean dot product on  $\mathbb{R}^d$  and  $[h]_n$  is the  $n$ -th row of  $h \in \mathbb{R}^{N \times d}$ . Importantly,  $[h_t]_n$  and  $[h^*]_n$  are set to have unit norm.

Mirroring (2), we can show the following proposition.

**Proposition 3.1** (Proof in Apx. A). *A necessary condition for (5) to reach a global optimum when  $\mathcal{V}$  is an average patch-wise similarity with unit length vectors is that for each  $x \in \mathcal{X}$  and  $t \in [0, 1]$ :*

$$(h_\theta \circ f_\theta)(x, t) = \mathbb{E}_{(x_0, x_1) \sim p_0 \times p_1} [\phi(x_0) \mid x_t = x]. \quad (6)$$

### 4. Guiding Generation at Inference

We perform inference by leveraging flow models trained with representation alignment, enabling generation conditioned on features  $\phi(x_c)$  from a reference image  $x_c$ . This approach is analogous to classifier guidance (Dhariwal & Nichol, 2021; Song et al., 2021b), but extends the paradigm to continuous features rather than discrete classes.

To generate samples  $x$  conditioned on  $\phi(x_c)$ , we introduce a guidance term that modifies the score function in (4) as:

$$\nabla_x \log p_t(x_t) + \lambda \nabla_x \mathcal{V}_x((h_\theta \circ f_\theta)(x_t, t), \phi(x_c)), \quad (7)$$

where  $\lambda > 0$  controls the influence of the conditioning signal. As formalized below, this modification is equivalent to sampling from the tilted distribution:

$$\tilde{p}_0(x; x_c) \propto p_0(x) e^{\lambda \mathcal{V}(\phi(x), \phi(x_c))}. \quad (8)$$

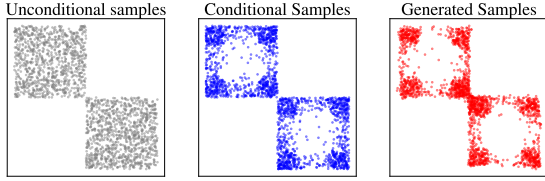


Figure 2. **Toy experiment.** Comparison of the target conditional distribution sampled via the rejection method (Devroye, 2006) versus our modified diffusion model. We provide additional analysis and implementation details in Appendix B.2.

To formalize our approach, we introduce the following assumptions on training convergence and energy landscapes.

**Assumption 4.1** (Global Optimality). We assume the model trained with  $\mathcal{L}^{\text{diff}}(\theta) + \beta\mathcal{L}^{\text{align}}(\theta)$  has reached a global optimum, such that the conditions (2) and (6) are satisfied.

**Assumption 4.2** (Vanishing Jensen Gap). Let  $Z_t(x; x_c) \triangleq \mathbb{E}_{(x_0, x_1) \sim p_0 \times p_1} [e^{\lambda\mathcal{V}(\phi(x_0), \phi(x_c))} \mid x_t = x]$  denote the log-expected energy at state  $x_t$ . By Jensen’s inequality:

$$\log Z_t(x; x_c) \geq \lambda \mathbb{E}_{(x_0, x_1)} [\mathcal{V}(\phi(x_0), \phi(x_c)) \mid x_t = x]. \quad (9)$$

We assume this bound is tight (i.e., the Jensen Gap vanishes).

We utilize the following Lemma, established by Rogers & Williams (2000); Didi et al. (2023), to connect modified SDEs to tilted distributions.

**Lemma 4.3** (Adapted from Didi et al. (2023) in Apx. B.1). *Given a backward SDE of the form  $dx_t = (v^*(x_t, t) - t\nabla_x \log p_t(x_t))dt + \sqrt{2t} d\bar{W}_t$  with  $x_1 \sim p_1$ , the reverse-time SDE:*

$$dx_t = (v^*(x_t, t) - t\nabla_x \log p_t(x_t) - 2t\nabla_x \log Z_t(x_t; x_c)) dt + \sqrt{2t} d\bar{W}_t, \quad (10)$$

satisfies  $\text{Law}(x_0) = \tilde{p}_0(\cdot; x_c)$ .

**Proposition 4.4** (Proof in Apx. B.1). *Assume  $\mathcal{V}(h, h^*) = \langle h, h^* \rangle$ . Under Assumptions 4.1 and 4.2, for a flow model  $v_\theta$  trained with representation alignment, the SDE:*

$$dx_t = (v^*(x_t, t) - t\nabla_x \log p_t(x_t) - 2\lambda t \nabla \mathcal{V}(x_t, \phi(x_c))) dt + \sqrt{2t} d\bar{W}_t, \quad (11)$$

with  $x_1 \sim p_1$ , produces samples distributed according to the tilted distribution  $\tilde{p}_0(x; x_c) \propto p_0(x)e^{\lambda\mathcal{V}(\phi(x), \phi(x_c))}$ .

**Toy Example.** We experimentally validate Proposition 4.4 using synthetic data. As shown in Figure 2, our model successfully samples from the target tilted distribution, sampled with rejection here. Details are provided in Appendix B.2.



Figure 3. **Impact of representation alignment on feature space.** We perform  $k$ -means clustering ( $k = 1,000$ ) on four feature spaces across ImageNet. For a reference image (with red frame), we visualize others from its assigned. Without alignment, SiT fails to form semantic groupings, making its latent space unsuitable for conditioning. In contrast, the aligned model successfully replicates the teacher’s semantic structure both before and after the projection layer, resulting in semantically consistent clusters.

## 5. Properties of Representation Space

We study how representation alignment (Yu et al., 2025) shapes the internal feature space of diffusion transformers and how this impacts feature conditioning. To this end, we use SiT models (Ma et al., 2024) trained on ImageNet (Deng et al., 2009). In this setting, the generation is done in the latent space of an autoencoder, but the visual backbone  $\phi$  takes as input images.

We argue that effective conditioning requires: (i) a semantically meaningful embedding space, where nearby embeddings correspond to similar concepts; and (ii) a smooth mapping from conditioning features to conditional distributions, so similar conditioning embeddings yield similar conditional densities.

**Representation alignment enables semantic features in diffusion transformers.** Self-supervised vision models learn rich representations from large-scale unlabeled data by enforcing invariance to augmentations while preserving semantic content. Among them, DINOv2 provides particularly strong semantic features and is widely used for representation alignment in diffusion models (Yu et al., 2025; Wang et al., 2025; Leng et al., 2025; Tian et al., 2025).

In contrast, the diffusion denoising objective alone rarely produces semantic features. Figure 3 highlights this difference: clustering ImageNet with DINOv2 features yields coherent, concept-level groups, whereas clustering SiT’s internal features produces clusters non-semantic clusters. Training SiT with a representation alignment loss restores semantic information in its internal feature space.

**Representation alignment ensures a well-conditioned mapping from features to image densities.** Following Kadkhodaie et al. (2025), we evaluate the Euclidean embedding property to ensure the conditioning space structure

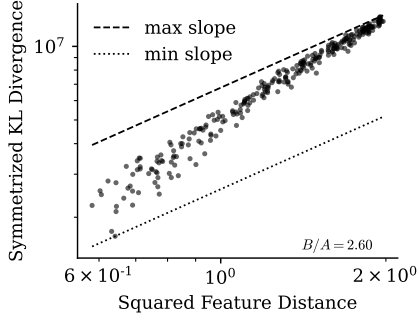


Figure 4. **Correlation between embedding and density distances.** The narrow range of the  $B/A$  ratio indicates a well-conditioned space where distances in any direction behave consistently.



Figure 5. **Semantic interpolation in the feature space.** Samples are generated by bilinearly interpolating the global conditioning features between four anchor images. The smooth transitions show the semantic coherence and stability of the mapping between the embedding space and conditional densities.

transfers to the conditional densities. This requires the distance  $d^2$  between the conditional densities  $p_1 = p(\cdot|\phi(x_1))$  and  $p_2 = p(\cdot|\phi(x_2))$  to scale with the squared distance between  $\phi(x_1)$ , and  $\phi(x_2)$ . Specifically, there must exist  $0 < A \leq B$  and  $B/A$  not too large such that for all  $x_1, x_2$ :

$$A\|\phi(x_1) - \phi(x_2)\|^2 \leq d^2(p_1, p_2) \leq B\|\phi(x_1) - \phi(x_2)\|^2 .$$

We define the density dissimilarity as:

$$d^2(p_1, p_2) = \frac{\lambda}{N} \sum_{n=1}^N \langle [\mathbb{E}_{p_1}[\phi(x)] - \mathbb{E}_{p_2}[\phi(x)]]_n, [\phi_1 - \phi_2]_n \rangle ,$$

which corresponds to the symmetrized Kullback-Leibler divergence under the sampling assumptions in Eq. (18) (see Appendix C.2 for details). Figure 4 shows a strong correlation between embedding and density distances, with a tight ratio  $B/A = 2.60$ , confirming the stability of the conditional space.

We further validate the semantic coherence of the embedding space and the smoothness of the density mapping in Figure 5 by interpolating between conditioning features. The resulting smooth transitions confirm the meaningful structure of the embedding space and its stable mapping to conditional densities.

## 6. Design choices for the Potential $\mathcal{V}$

We have presented a guidance method for test-time visual conditioning within the representatively aligned class of diffusion models. While Section 3 outlined the required properties of the feature extractor  $\phi$ , the model is specifically trained to align with the potential:

$$\mathcal{V}(h, h^*) = \frac{1}{N} \sum_{n=1}^N \langle [h]_n, [h^*]_n \rangle , \quad (12)$$

where  $h, h^* \in \mathbb{R}^{N \times d}$ . In this section, we discuss how (12) can be adapted during inference to achieve specific characteristics in the generated images.

### 6.1. Guidance via Independent Patch Alignment (IPA)

Eq. (12) can be generalized to allow for spatial flexibility:

$$\mathcal{V}_P(h, h^*) = \sum_{n=1}^N \sum_{m=1}^N P_{n,m} \langle [h]_n, [h^*]_m \rangle , \quad (13)$$

where  $P \in \mathbb{R}^{N \times N}$  is a weight matrix such that  $P_{n,m}$  defines the interaction strength between predicted patch  $n$  and conditioning patch  $m$ , normalized such that  $\sum_n \sum_m P_{n,m} = 1$ . By manipulating  $P$ , we achieve fine-grained control over the generation process. Because  $P$  is determined independently of the feature alignments, we refer to this class of conditioning as *Independent Patch Alignment (IPA)*. We detail three specific configurations of  $P$  below.

**Alignment with full feature map.** Setting  $P = \frac{1}{N}I$  recovers the original alignment objective (12). This configuration enforces a dense, spatial constraint, resulting in a stochastic reconstruction of the conditioning image.

**Alignment with feature mask.** When only specific regions of the conditioning image are relevant, we define a binary mask  $m \in \{0, 1\}^N$  and its corresponding index set  $\mathcal{S} = \{n \mid m_n = 1\}$ . The weights are defined as  $P_{n,m} = \frac{1}{|\mathcal{S}|} \mathbf{1}[m = n] \mathbf{1}[n \in \mathcal{S}]$ . This *masked-conditioning* potential preserves information within the masked region while allowing for structural variation in the surrounding areas.

**Alignment with an average concept.** To steer generation toward the global semantic content of a reference image without enforcing pixel-wise spatial fidelity, we utilize an *average-concept* potential. Here, we set  $P_{n,m} = \frac{1}{N^2 \|\bar{h}\| \|\bar{h}^*\|}$ , which is equivalent to aligning the spatial average of the predicted features with the spatial average of the conditioning features,  $\bar{h}^*$ . This preserves the general semantic category while removing all spatial constraints.

Table 1. **Distribution-level comparison of REPA-G generations on ImageNet (Deng et al., 2009).** We compare the standard SiT backbone (Ma et al., 2024) (no representation alignment) against REPA (Wang et al., 2025) and REPA-E (Leng et al., 2025) variants. For each method block, the first row denotes results for unconditional generation, serving as a baseline, and  $F_{\text{SiT}}$  and  $F_{\text{DINO}}$  for REPA-G.

Model	Cond.	Full Feature Map					Masked Feature Map					Average Feature Map				
		FID↓	sFID↓	IS↑	Prec.↑	Rec.↑	FID↓	sFID↓	IS↑	Prec.↑	Rec.↑	FID↓	sFID↓	IS↑	Prec.↑	Rec.↑
SiT	-	<b>45.02</b>	<b>9.02</b>	<b>22.33</b>	<b>0.50</b>	<b>0.63</b>	<b>45.02</b>	<b>9.02</b>	22.33	<b>0.50</b>	<b>0.63</b>	<b>45.02</b>	<b>9.02</b>	<b>22.33</b>	<b>0.50</b>	<b>0.63</b>
	$F_{\text{SiT}}$	71.35	72.08	14.73	0.33	0.54	45.85	19.23	<b>29.36</b>	0.40	0.62	65.99	22.52	16.69	0.36	0.52
REPA	-	26.58	6.85	41.31	0.56	<b>0.70</b>	26.58	6.85	41.31	0.56	<b>0.70</b>	26.58	6.85	41.31	0.56	<b>0.70</b>
	$F_{\text{DINO}}$	7.23	8.86	199.69	0.65	0.69	14.17	10.59	135.08	0.58	0.64	29.06	16.79	83.85	0.46	0.69
	$F_{\text{SiT}}$	<b>2.09</b>	<b>6.17</b>	<b>260.97</b>	<b>0.74</b>	<b>0.70</b>	<b>2.67</b>	<b>4.86</b>	<b>222.71</b>	<b>0.74</b>	0.69	<b>6.26</b>	<b>6.14</b>	<b>159.14</b>	<b>0.68</b>	<b>0.70</b>
REPA-E	-	15.07	4.46	55.14	0.65	<b>0.69</b>	15.07	4.46	55.14	0.65	<b>0.69</b>	15.07	<b>4.46</b>	55.14	0.65	<b>0.69</b>
	$F_{\text{DINO}}$	<b>1.45</b>	<b>4.07</b>	<b>264.69</b>	<b>0.76</b>	<b>0.69</b>	2.30	4.84	212.25	0.75	0.67	3.24	5.20	188.92	0.73	0.67
	$F_{\text{SiT}}$	2.15	6.64	264.48	0.75	0.68	<b>1.79</b>	<b>4.13</b>	<b>237.37</b>	<b>0.76</b>	0.68	<b>2.50</b>	4.81	<b>201.13</b>	<b>0.74</b>	<b>0.69</b>

Table 2. **Instance-level comparison of REPA-G generations on ImageNet (Deng et al., 2009).** Setup is the same as in Table 1. Alignment is measured with DINOv2 (Oquab et al., 2024), JEPa (Assran et al., 2023), and CLIP (Radford et al., 2021) feature spaces, supplemented by PSNR for pixel-level fidelity. We highlight ours conditioning methods with  $F_{\text{SiT}}$  and  $F_{\text{DINO}}$ .

Model	Cond.	Full Feature Map				Masked Feature Map				Average Feature Map			
		DINOv2	JEPa	CLIP	PSNR	DINOv2	JEPa	CLIP	PSNR	DINOv2	JEPa	CLIP	PSNR
SiT	$F_{\text{SiT}}$	0.27	0.36	0.43	15.35	0.44	0.48	0.46	17.98	0.12	0.35	0.83	7.74
REPA	$F_{\text{DINO}}$	0.75	0.61	0.58	11.02	0.77	0.60	0.57	10.63	0.76	0.69	0.92	8.00
	$F_{\text{SiT}}$	<b>0.85</b>	<b>0.78</b>	<b>0.71</b>	<b>20.46</b>	<b>0.87</b>	<b>0.79</b>	<b>0.71</b>	<b>20.72</b>	<b>0.84</b>	<b>0.84</b>	<b>0.95</b>	<b>10.82</b>
REPA-E	$F_{\text{DINO}}$	0.83	0.69	0.64	15.23	0.85	0.68	0.63	14.36	<b>0.91</b>	0.83	<b>0.96</b>	10.97
	$F_{\text{SiT}}$	<b>0.86</b>	<b>0.76</b>	<b>0.71</b>	<b>18.68</b>	<b>0.88</b>	<b>0.78</b>	<b>0.71</b>	<b>19.07</b>	<b>0.91</b>	<b>0.88</b>	<b>0.96</b>	<b>11.96</b>

**Alignment with a single concept.** Alternatively, we consider *single-concept* alignment, where the full generated feature map is compared against a single target patch  $i$ . This corresponds to  $P_{n,m} = \frac{1}{N} \mathbf{1}[m = i]$ , focusing the guidance signal on a local feature from the conditioning image.

## 6.2. Guidance via Selective Patch Alignment (SPA)

While IPA uses constant weighting, *Selective Patch Alignment* dynamically weights predicted patches based on their similarity to a target concept  $h_i^*$ , as follows:

$$\psi^{\text{SPA}}(h, h^*) = T \log \left[ \sum_{n=1}^N \exp \left( \frac{\langle [h]_n, [h^*]_i \rangle}{T} \right) \right], \quad (14)$$

where the temperature  $T$  modulates selection sparsity. As  $T \rightarrow 0$ , the potential recovers a hard-maximum over patches; as  $T \rightarrow \infty$ , it converges to the uniform average-concept baseline. This soft-maximum mechanism allows the model to adaptively localize concepts, bypassing the rigid spatial constraints of the conditioning image. More intuition and theoretical justifications are in the Appendix D.1.

## 7. Experiments

**Datasets.** We evaluate on ImageNet (Deng et al., 2009), which contains 1.2M images across 1,000 classes, and on COCO (Lin et al., 2014), which includes 123K images. Both datasets are preprocessed to a resolution of 256×256.

**Implementation Details.** We set the hyperparameter  $\lambda$  in (7) to 50,000 and the PCA threshold for mask extraction to 0.5. We follow Ma et al. (2024) by using a SDE integrated via the Euler-Maruyama solver with 250 steps.

We evaluate the performance of our proposed test-time visual feature guidance mechanisms by analyzing their generated outputs. For our experiments, we use a pretrained flow matching models with representation alignment on the ImageNet. Using this framework, we first evaluate the conditional generation capabilities of REPA-G across varying granularities of feature types. We then explore the ability of our method to compose features from multiple images.

### 7.1. Test-time Guidance with Single Source

In this series of experiments, we use a single "anchor image" whose features guide the generation process. We generate images using guidance mechanisms derived from Independent Patch Alignment (IPA), including: (i) Full Feature Map, utilizing all patch features; (ii) Masked Feature Map, utilizing a subset of patch features; and (iii) Average Feature Map, utilizing the global average of all patch features. To generate the masked feature maps, we extract DINOv2 (Oquab et al., 2024) patch features, compute the first principal component, and apply a threshold to isolate the foreground.

We conduct our evaluations across three unconditional flow matching models: a standard SiT-XL (Ma et al., 2024)

Table 3. **Distribution-level zero-shot evaluation on the COCO (Lin et al., 2014) dataset.** The setup is the same as in Table 1. Within each block, the first row reports unconditional generation results as a baseline, while  $F_{\text{SiT}}$  and  $F_{\text{DINO}}$  denote our method.

Model	Cond.	Full Feature Map					Masked Feature Map					Average Feature Map				
		FID↓	sFID↓	IS↑	Prec.↑	Rec.↑	FID↓	sFID↓	IS↑	Prec.↑	Rec.↑	FID↓	sFID↓	IS↑	Prec.↑	Rec.↑
SiT	-	<b>45.13</b>	<b>30.15</b>	<b>22.33</b>	<b>0.42</b>	<b>0.54</b>	<b>45.13</b>	<b>30.15</b>	<b>22.33</b>	<b>0.42</b>	<b>0.54</b>	<b>45.13</b>	<b>30.15</b>	<b>22.33</b>	<b>0.42</b>	<b>0.54</b>
	$F_{\text{SiT}}$	77.26	108.79	9.86	0.25	0.37	51.88	42.36	15.76	0.27	0.52	66.09	46.88	16.67	0.28	0.45
REPA	-	37.85	29.11	41.31	0.45	0.58	37.85	29.11	41.31	0.45	0.58	37.85	29.11	41.31	0.45	0.58
	$F_{\text{DINO}}$	12.96	29.05	31.11	0.55	0.57	20.51	31.04	26.15	0.45	0.53	32.04	39.05	20.59	0.35	0.53
	$F_{\text{SiT}}$	<b>6.18</b>	<b>25.35</b>	<b>33.08</b>	<b>0.65</b>	<b>0.62</b>	<b>6.63</b>	<b>24.37</b>	<b>32.05</b>	<b>0.65</b>	<b>0.61</b>	<b>9.46</b>	<b>25.89</b>	<b>29.43</b>	<b>0.60</b>	<b>0.60</b>
REPA-E	-	36.23	29.98	55.13	0.51	0.59	36.23	29.98	55.13	0.51	0.59	36.23	29.98	55.13	0.51	0.59
	$F_{\text{DINO}}$	<b>4.61</b>	<b>23.27</b>	<b>35.97</b>	<b>0.67</b>	<b>0.64</b>	5.65	23.35	34.54	0.64	0.63	6.07	24.09	32.76	0.63	<b>0.63</b>
	$F_{\text{SiT}}$	5.70	25.55	34.29	0.66	0.62	<b>4.92</b>	<b>23.03</b>	<b>34.78</b>	<b>0.66</b>	<b>0.63</b>	<b>5.45</b>	<b>23.98</b>	<b>33.81</b>	<b>0.64</b>	<b>0.63</b>

Table 4. **Comparison with text-to-image (T2I) generation.** We compare our method against CAD-I (Degeorge et al., 2025), an ImageNet-trained T2I baseline, using COCO validation captions as conditioning signals. Our method utilizes full and average feature maps extracted from REPA-E (Leng et al., 2025).

Model	Cond.	FID ↓	sFID ↓	IS ↑	Prec. ↑	Rec. ↑
CAD-I	Text	37.98	29.87	25.60	0.46	0.37
REPA-E	Avg. Feat.	3.58	11.10	32.69	0.75	0.78
REPA-E	Full Feat.	<b>2.11</b>	<b>8.35</b>	<b>36.01</b>	<b>0.98</b>	<b>0.96</b>

(trained without representation alignment), REPA (Wang et al., 2025) and REPA-E (Leng et al., 2025), both trained with representation alignment. For conditioning, we extract internal features ( $F_{\text{SiT}}$ ), at  $t = 0$ , from the same backbone layer across all models, specifically the layer before the projection layer used in the REPA variants, i.e.  $f_{\theta}(x_t, t)$ . For the REPA-based models, we also evaluated features extracted after the projection layer (i.e.  $h_{\theta}(f_{\theta}(x_t, t))$ ) but observed no significant difference in performance; further details are provided in Appendix E.1. Additionally, for the REPA and REPA-E models, we extend our evaluation to include DINOv2 features ( $F_{\text{DINO}}$ ) as an external conditioning.

**Distribution-level evaluation.** We first evaluate the generated outputs at the distribution level using standard metrics, FID (Heusel et al., 2017), sFID (Nash et al., 2021), IS (Salimans et al., 2016), Precision, and Recall (Kynkäänniemi et al., 2019). Distribution level evaluation is non-trivial, as a clear target conditional density is unavailable. To address this, we approximate the unconditional target distribution by aggregating the conditional densities across anchor features. We define these conditional densities using three feature granularities: (i) full feature maps, (ii) masked feature maps, and (iii) average features. These conditioning signals are extracted from 50,000 anchor images sampled uniformly across all classes from the ImageNet training set. Using these anchor features, we generate 50,000 images via test-time conditioning and compare them against statistics computed on the whole dataset.

We report results on ImageNet (Table 1) and present a zero-

shot evaluation on COCO (Table 3) using the same models. The first rows show that SiT does not respond well on REPA-G due to an ambiguous feature space, as the FID increases when applying IPA. In contrast, REPA and REPA-E benefit from DINOv2 feature alignment, allowing them to better react to the conditioning across all granularity levels.

**Instance-level evaluation.** To verify that the generated samples follow the given conditions, we evaluate quality at the instance level using feature extractors DINOv2 (Oquab et al., 2024), JEPa (Assran et al., 2023), and CLIP (Radford et al., 2021). We compute the average alignment score (i.e., cosine similarity) between the features of each anchor image and the corresponding generated image across three granularities. For the average feature map, alignment is calculated between global average features; for the full feature map, it is computed as the mean of all patch-wise similarities; and for the masked setup, it is the mean of patch similarities within the masked region. Furthermore, we report PSNR to measure the low-level pixel fidelity.

The results in Table 2 indicate that achieving high similarity to the anchor images requires a well-structured representation space. The vanilla SiT model fails to follow the anchor images, whereas REPA and REPA-E nearly perfectly reconstruct the condition across all levels of granularity.

**Comparison with text-to-image.** We also compare our model against the text-to-image (T2I) model CAD-I (Degeorge et al., 2025) as a baseline in Table 4. Unlike most T2I models trained on massive, scene-centric datasets, CAD-I is specifically trained on ImageNet. For this evaluation, we use long captions extracted by Degeorge et al. (2025) from the COCO validation set as conditioning signals for CAD-I to generate the described scenes. For our method, we utilize both full and average feature maps extracted from the internal SiT representations before the projection layer trained with REPA-E to generate the corresponding images. The performance gap between text-to-image and visual feature conditioning shows that visual features provide a denser, more informative signal than text captions.

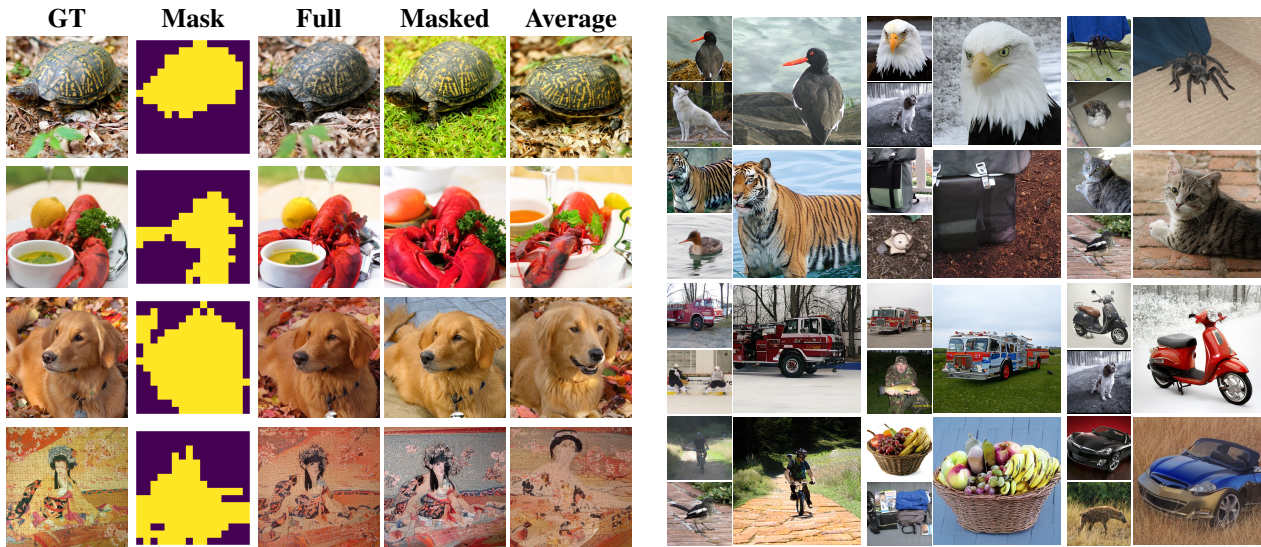


Figure 6. Qualitative comparison on ImageNet (Deng et al., 2009) using REPA-E (Leng et al., 2025) with DINOv2 features. (Left) We show single-source conditioning across three levels of granularity: full, masked, and averaged feature maps. (Right) We illustrate multi-source composition. Within each group, the anchor object and target background are shown at a small scale alongside the enlarged generation. We use full features from the anchor and a single feature patch sampled from the target’s background.

Table 5. Compositional generation evaluation on ImageNet (Deng et al., 2009). We assess visual quality with PickScore and concept adherence using CLIP, and compare REPA-G variants using IPA and SPA against standard baselines.

Cond.	Pick Score	CLIP Score	Target Sim.	Anchor Sim.	Combined Sim.
Uncond.	0.175	0.100	0.098	0.113	0.105
Class Cond.	<b>0.198</b>	0.220	0.110	0.243	0.177
Interp.	0.188	0.190	0.156	0.183	0.170
IPA→IPA	<u>0.196</u>	<u>0.232</u>	<u>0.372</u>	<b>0.452</b>	<u>0.412</u>
IPA→SPA	<u>0.196</u>	<b>0.238</b>	<b>0.510</b>	<u>0.422</u>	<b>0.466</b>

## 7.2. Test-time Guidance with Multiple Sources

We evaluate concept-blending by composing anchor images (source objects) with target features (backgrounds). We apply two successive conditioning steps: first, an object-level IPA using the anchor’s DINO features, followed by a target background condition implemented via IPA or SPA. The resulting images should preserve the anchor object while adopting the target background’s characteristics. We evaluate on a 50-class ImageNet subset representing diverse objects. For each class, 100 random samples are combined with 8 hand-selected target background features, yielding 40,000 images per method.

As novel image compositions are steering away from the real distribution, FID is inapplicable. We therefore evaluate image quality via Pick Score (Kirstain et al., 2023) and concept adherence via CLIP Score (Hessel et al., 2021), using the prompt: *An image of a/an [Anchor Class] with a [Target Class] background.* Additionally, we introduce patch-wise similarity metrics: each generated patch is assigned to the

anchor or target based on maximum cosine similarity. We then compute Anchor, Target, and Combined similarities to quantify feature adherence to each source.

We compare our method against three baselines: (i) unconditional, (ii) class-conditional (using the anchor class), and (iii) interpolated conditional generation, which blends class embeddings via adapted Classifier-Free Guidance. Our compositional conditioning is evaluated using two variants: IPA followed by IPA (IPA→IPA) and IPA followed by SPA (IPA→SPA). As shown in Table 5, REPA-G significantly outperforms baselines in prompt alignment and image quality. While class-conditional baselines are limited by an inability to encode specific target backgrounds (e.g., a tiger with a water background), REPA-G leverages DINO features to achieve superior anchor and target alignment. Notably, the SPA variant is most effective at blending sources, yielding the highest CLIP Score (see Appendix E.4). Figure 6 shows qualitative results.

## 8. Conclusion

We introduced REPA-G, an inference-time framework that leverages aligned self-supervised representations to condition diffusion models. By guiding the sampling process, REPA-G enables semantic control without the need for re-training. While effective, our approach currently requires tuning  $\lambda$  to balance concepts in compositional generation. Furthermore, feature alignment is more difficult when dealing with varying scene viewpoints. Addressing these limitations and integrating our guidance with orthogonal conditioning methods remain a promising research direction.

## ACKNOWLEDGMENT

We acknowledge EuroHPC Joint Undertaking for awarding the project ID EHPC-REG-2024R02-234 access to Karolina, Czech Republic.

## References

- Assran, M., Duval, Q., Misra, I., Bojanowski, P., Vincent, P., Rabat, M. G., LeCun, Y., and Ballas, N. Self-supervised learning from images with a joint-embedding predictive architecture. *CVPR*, 2023.
- Chen, X., Xie, S., and He, K. An empirical study of training self-supervised vision transformers. In *ICCV*, 2021.
- Couairon, G., Verbeek, J., Schwenk, H., and Cord, M. Diffedit: Diffusion-based semantic image editing with mask guidance. In *ICLR*, 2023.
- Degeorge, L., Ghosh, A., Dufour, N., Picard, D., and Kalogeiton, V. How far can we go with imagenet for text-to-image generation? *arXiv preprint arXiv:2502.21318*, 2025.
- Deng, J., Dong, W., Socher, R., Li, L.-J., Li, K., and Fei-Fei, L. Imagenet: A large-scale hierarchical image database. In *CVPR*, 2009.
- Devroye, L. Chapter 4 nonuniform random variate generation. In Henderson, S. G. and Nelson, B. L. (eds.), *Simulation*, Handbooks in Operations Research and Management Science. Elsevier, 2006.
- Dhariwal, P. and Nichol, A. Diffusion models beat gans on image synthesis. *NeurIPS*, 2021.
- Didi, K., Vargas, F., Mathis, S., Dutordoir, V., Mathieu, E., Komorowska, U. J., and Lio, P. A framework for conditional diffusion modelling with applications in motif scaffolding for protein design. In *NeurIPS 2023 Workshop*, 2023.
- Douze, M., Guzhva, A., Deng, C., Johnson, J., Szilvassy, G., Mazaré, P.-E., Lomeli, M., Hosseini, L., and Jégou, H. The faiss library. *IEEE Transactions on Big Data*, 2025.
- Efron, B. Tweedie’s formula and selection bias. *Journal of the American Statistical Association*, 2011.
- Esser, P., Kulal, S., Blattmann, A., Entezari, R., Müller, J., Saini, H., Levi, Y., Lorenz, D., Sauer, A., Boesel, F., et al. Scaling rectified flow transformers for high-resolution image synthesis. In *ICML*, 2024.
- Fokker, A. D. Die mittlere energie rotierender elektrischer dipole im strahlungsfeld. *Annalen der Physik*, 1914.
- Goodfellow, I., Pouget-Abadie, J., Mirza, M., Xu, B., Warde-Farley, D., Ozair, S., Courville, A., and Bengio, Y. Generative adversarial networks. *NeurIPS*, 2014.
- He, K., Chen, X., Xie, S., Li, Y., Dollár, P., and Girshick, R. Masked autoencoders are scalable vision learners. In *CVPR*, 2022.
- Hertz, A., Mokady, R., Tenenbaum, J., Aberman, K., Pritch, Y., and Cohen-Or, D. Prompt-to-prompt image editing with cross-attention control. In *ICLR*, 2023.
- Hessel, J., Holtzman, A., Forbes, M., Le Bras, R., and Choi, Y. Clipscore: A reference-free evaluation metric for image captioning. In *EMNLP*, 2021.
- Hessel, J., Holtzman, A., Forbes, M., Bras, R. L., and Choi, Y. Clip-score: A reference-free evaluation metric for image captioning. *arXiv preprint arXiv:2104.08718*, 2022.
- Heusel, M., Ramsauer, H., Unterthiner, T., Nessler, B., and Hochreiter, S. Gans trained by a two time-scale update rule converge to a local nash equilibrium. In *NeurIPS*, 2017.
- Ho, J. and Salimans, T. Classifier-free diffusion guidance. *arXiv preprint arXiv:2207.12598*, 2022.
- Ho, J., Jain, A., and Abbeel, P. Denoising Diffusion Probabilistic Models. In *NeurIPS*, 2020.
- Kadkhodaie, Z., Mallat, S., and Simoncelli, E. Elucidating the representation of images within an unconditional diffusion model denoiser. *arXiv preprint arXiv:2506.01912*, 2025.
- Karras, T., Aittala, M., Hellsten, J., Laine, S., Lehtinen, J., and Aila, T. Training generative adversarial networks with limited data. *NeurIPS*, 2020.
- Kingma, D. P. Adam: A method for stochastic optimization. *ICLR*, 2015.
- Kingma, D. P. and Welling, M. Auto-encoding variational bayes. *arXiv preprint arXiv:1312.6114*, 2013.
- Kirstain, Y., Polyak, A., Singer, U., Matiana, S., Penna, J., and Levy, O. Pick-a-pic: An open dataset of user preferences for text-to-image generation. *NeurIPS*, 2023.
- Kynkäänniemi, T., Karras, T., Laine, S., Lehtinen, J., and Aila, T. Improved precision and recall metric for assessing generative models. *NeurIPS*, 2019.
- Labs, B. F. Flux. <https://github.com/black-forest-labs/flux>, 2024.
- Labs, B. F., Batifol, S., Blattmann, A., Boesel, F., Consul, S., Diagne, C., Dockhorn, T., English, J., English, Z., Esser, P., Kulal, S., Lacey, K., Levi, Y., Li, C., Lorenz, D., Müller, J., Podell, D., Rombach, R., Saini, H., Sauer, A., and Smith, L. Flux.1 kontext: Flow matching for in-context image generation and editing in latent space. *arXiv preprint arXiv:2506.15742*, 2025.
- Leng, X., Singh, J., Hou, Y., Xing, Z., Xie, S., and Zheng, L. REPA-E: Unlocking VAE for End-to-End Tuning with Latent Diffusion Transformers. *arXiv preprint arXiv:2504.10483*, 2025.
- Lin, T.-Y., Maire, M., Belongie, S., Hays, J., Perona, P., Ramanan, D., Dollár, P., and Zitnick, C. L. Microsoft coco: Common objects in context. In *ECCV*, 2014.
- Lipman, Y., Chen, R. T., Ben-Hamu, H., Nickel, M., and Le, M. Flow matching for generative modeling. In *ICLR*, 2023.
- Ma, N., Goldstein, M., Albergo, M. S., Boffi, N. M., Vanden-Eijnden, E., and Xie, S. Sit: Exploring flow and diffusion-based generative models with scalable interpolant transformers. In *ECCV*, 2024.
- Nash, C., Menick, J., Dieleman, S., and Battaglia, P. Generating images with sparse representations. In *ICML*, 2021.

- Oquab, M., Darcet, T., Moutakanni, T., Vo, H. V., Szafraniec, M., Khalidov, V., Fernandez, P., HAZIZA, D., Massa, F., El-Nouby, A., Assran, M., Ballas, N., Galuba, W., Howes, R., Huang, P.-Y., Li, S.-W., Misra, I., Rabbat, M., Sharma, V., Synnaeve, G., Xu, H., Jegou, H., Mairal, J., Labatut, P., Joulin, A., and Bojanowski, P. DINOv2: Learning robust visual features without supervision. *TMLR*, 2024.
- Peebles, W. and Xie, S. Scalable diffusion models with transformers. In *ICCV*, 2023.
- Planck, M. Ueber einen satz der statistischen dynamik und eine erweiterung in der quantumtheorie sitz. ber. *Preussischen Akad. Wiss*, 1917.
- Radford, A., Kim, J. W., Hallacy, C., Ramesh, A., Goh, G., Agarwal, S., Sastry, G., Askell, A., Mishkin, P., Clark, J., et al. Learning transferable visual models from natural language supervision. In *ICML*, 2021.
- Rogers, L. C. G. and Williams, D. *Diffusions, Markov processes, and martingales*, volume 2. Cambridge university press, 2000.
- Rombach, R., Blattmann, A., Lorenz, D., Esser, P., and Ommer, B. High-Resolution Image Synthesis with Latent Diffusion Models. In *CVPR*, 2022.
- Saharia, C., Chan, W., Saxena, S., Li, L., Whang, J., Denton, E. L., Ghasemipour, K., Gontijo Lopes, R., Karagol Ayan, B., Salimans, T., et al. Photorealistic text-to-image diffusion models with deep language understanding. *NeurIPS*, 2022.
- Salimans, T., Goodfellow, I., Zaremba, W., Cheung, V., Radford, A., and Chen, X. Improved techniques for training generative adversarial networks. In *NeurIPS*, 2016.
- Serejjo-Garros, N., Kirby, E., Besnier, V., and Samet, N. Leveraging 3d representation alignment and rgb pretrained priors for lidar scene generation. In *ICRA*, 2026.
- Singh, J., Leng, X., Wu, Z., Zheng, L., Zhang, R., Shechtman, E., and Xie, S. What Matters for Representation Alignment: Global Information or Spatial Structure? *arXiv preprint arXiv:2512.10794*, 2025.
- Song, J., Meng, C., and Ermon, S. Denoising diffusion implicit models. In *ICLR*, 2021a.
- Song, Y., Sohl-Dickstein, J., Kingma, D. P., Kumar, A., Ermon, S., and Poole, B. Score-based generative modeling through stochastic differential equations. In *ICLR*, 2021b.
- Stracke, N., Baumann, S. A., Susskind, J., Bautista, M. A., and Ommer, B. Ctrloralter: conditional loradapter for efficient 0-shot control and altering of t2i models. In *ECCV*, 2024.
- Tian, Y., Chen, H., Zheng, M., Liang, Y., Xu, C., and Wang, Y. U-REPA: Aligning Diffusion U-Nets to ViTs. *arXiv preprint arXiv:2503.18414*, 2025.
- Wang, Z., Zhao, W., Zhou, Y., Li, Z., Liang, Z., Shi, M., Zhao, X., Zhou, P., Zhang, K., Wang, Z., Wang, K., and You, Y. REPA Works Until It Doesn't: Early-Stopped, Holistic Alignment Supercharges Diffusion Training. *arXiv preprint arXiv:2505.16792*, 2025.
- Xie, S., Zhang, Z., Lin, Z., Hinz, T., and Zhang, K. Smartbrush: Text and shape guided object inpainting with diffusion model. In *CVPR*, 2023.
- Yang, B., Gu, S., Zhang, B., Zhang, T., Chen, X., Sun, X., Chen, D., and Wen, F. Paint by example: Exemplar-based image editing with diffusion models. In *CVPR*, 2023.
- Yao, J., Yang, B., and Wang, X. Reconstruction vs. Generation: Taming Optimization Dilemma in Latent Diffusion Models. In *CVPR*, 2025.
- Ye, H., Zhang, J., Liu, S., Han, X., and Yang, W. Ip-adapter: Text compatible image prompt adapter for text-to-image diffusion models. *arXiv preprint arxiv:2308.06721*, 2023.
- Yu, S., Kwak, S., Jang, H., Jeong, J., Huang, J., Shin, J., and Xie, S. Representation alignment for generation: Training diffusion transformers is easier than you think. *ICLR*, 2025.
- Zhang, L., Rao, A., and Agrawala, M. Adding conditional control to text-to-image diffusion models. In *ICCV*, 2023.

This appendix supplements the main paper with additional details regarding the preliminaries (Section 3), guiding generation at inference (Section 4), and representation space properties (Section 5). We also elaborate on the design of the potential  $\mathcal{V}$  (Section 6). Finally, we provide extended quantitative and qualitative results for both the ImageNet (Deng et al., 2009) and COCO (Lin et al., 2014) datasets.

**To support reproducibility**, we provide the implementation for our toy example in the supplementary material. Upon acceptance, we will release our full codebase and pre-trained models to the public.

## A. Complementary Details on Preliminaries (Section 3)

We use the notation established in Section 3. Below, we provide the derivation for Proposition 6, assuming  $N = 1$  without loss of generality.

**Proof of Proposition 6.** The potential  $\mathcal{V}$  can be expressed in terms of the  $L_2$  distance as follows:

$$\begin{aligned} \mathcal{V}((h_\theta \circ f_\theta)(x_t, t), \phi(x_0)) &= \langle (h_\theta \circ f_\theta)(x_t, t), \phi(x_0) \rangle \\ &= 1 - \frac{1}{2} \|(h_\theta \circ f_\theta)(x_t, t) - \phi(x_0)\|_2^2, \end{aligned}$$

where the second equality holds because the vectors in the scalar product are constrained to unit length. Consequently, minimizing the alignment loss  $\mathcal{L}^{\text{align}}$  defined in (5) is equivalent to minimizing the following objective over  $\theta$ :

$$\mathbb{E}_{\substack{t \sim \mathcal{U}(0,1) \\ (x_0, x_1) \sim p_0 \times p_1}} \left[ \|(h_\theta \circ f_\theta)(x_t, t) - \phi(x_0)\|_2^2 \right].$$

From the properties of conditional expectation in minimum mean square error (MMSE) estimation, this quantity is minimized when, for every  $x \in \mathcal{X}$  and  $t \in [0, 1]$ :

$$(h_\theta \circ f_\theta)(x, t) = \mathbb{E}_{x_0, x_1 \sim p_0 \times p_1} [\phi(x_0) \mid (1-t)x_0 + tx_1 = x].$$

□

## B. Complementary Details on Guiding Generation at Inference (Section 4)

### B.1. Sampling from the tilted distribution

Let us consider the following forward time SDE

$$dx_t = (v^*(x_t, t) + t \nabla_x \log p_t(x_t)) dt + \sqrt{2t} dW_t. \quad (15)$$

Starting from the Fokker-Plank equation (Fokker, 1914; Planck, 1917), we have:

$$\begin{aligned} \frac{\partial p_t}{\partial t} &= -\nabla \cdot (p_t(v_t^* + t \nabla \log p_t)) + t \Delta p_t \\ &= -\nabla \cdot (p_t v_t^*) - \nabla \cdot (t p_t \nabla \log p_t) + t \Delta p_t \\ &= -\nabla \cdot (p_t v_t^*) - \nabla \cdot (t \nabla p_t) + t \Delta p_t \\ &= -\nabla \cdot (p_t v_t^*) - t \Delta p_t + t \Delta p_t \\ &= -\nabla \cdot (p_t v_t^*). \end{aligned}$$

We see that the forward SDE (15) shares the same marginals as the ODE  $\dot{x}_t = v^*(x_t, t)$ , which we use during the forward.

### Proof of Lemma 4.3..

Consider the forward SDE (15), where the marginals  $p_t$  are induced by the interpolation process  $x_t = \alpha_t x_0 + \sigma_t x_1$ , with  $x_0 \sim p_0$  and  $x_1 \sim p_1$ . We define the tilting term  $p(\phi(x_c) \mid x_0) = e^{\lambda \mathcal{V}(\phi(x_0), \phi(x_c))}$  and the corresponding time-dependent potential  $Z_t(x; x_c) \triangleq \mathbb{E}_{x_0 \sim p(x_0 \mid x_t)} [e^{\lambda \mathcal{V}(\phi(x_0), \phi(x_c))} \mid x_t = x]$ . Applying Proposition 2.3. from Didi et al. (2023), the reverse-time SDE is given by:

$$\begin{aligned} dx_t &= (v^*(x_t, t) + t \nabla_x \log p_t(x_t) - 2t(\nabla_x \log p_t(x_t) + \nabla_x \log Z_t(x; x_c))) dt + \sqrt{2t} d\bar{W}_t \\ &= (v^*(x_t, t) - t(\nabla_x \log p_t(x_t) + 2\nabla_x \log Z_t(x; x_c))) dt + \sqrt{2t} d\bar{W}_t \end{aligned}$$

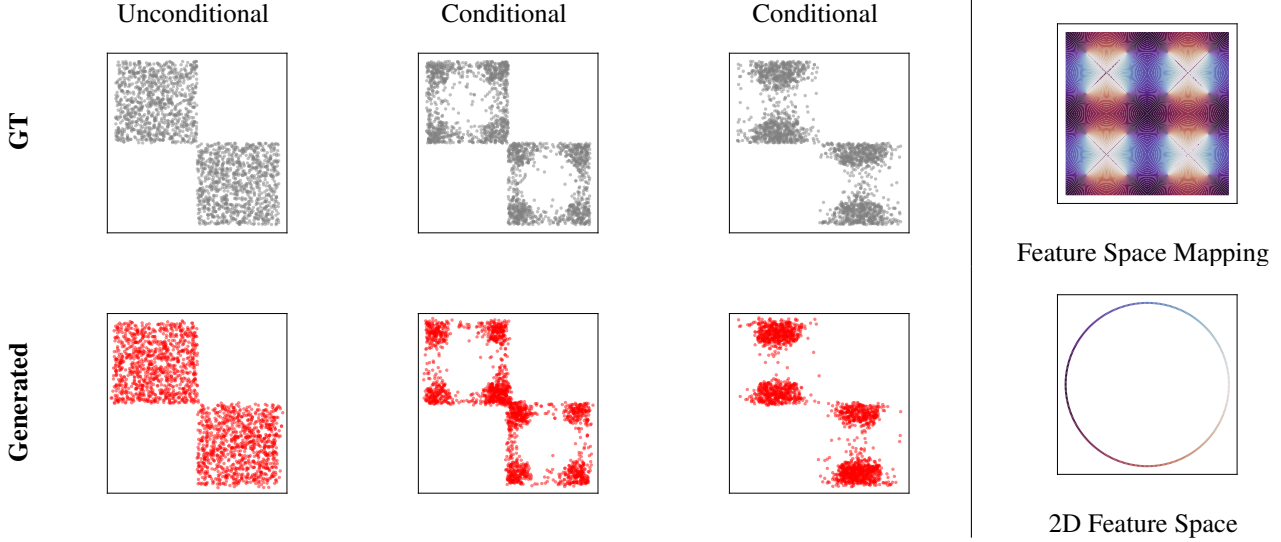


Figure 7. **Representation alignment with diffusion in 2D space.** Ground-truth samples are shown in grey, with corresponding samples generated via diffusion in red. The conditional results in the second and third columns are guided by target feature vectors  $[-1, 0]$  and  $[0, -1]$ , respectively. The last column shows the feature space mapping, mapping each data points to its corresponding 2D feature.

Initialised at  $x_1 \sim p_1$ , this SDE yields samples  $x_0 \sim \tilde{p}_0(x; x_c) \propto p_0(x)e^{\lambda \mathcal{V}(\phi(x), \phi(x_c))}$ , effectively sampling from the tilted distribution.  $\square$

**Proof of Proposition 4.4.** By Assumption 4.1, the optimality condition (6) holds, which implies that the network recovers the conditional expectation:  $f_\theta(x, t) = \mathbb{E}_{(x_0, x_1) \sim p_0 \times p_1}[\phi(x_0) \mid x_t = x]$ . Consequently:

$$\mathcal{V}(f_\theta(x, t), \phi(x_c)) = \mathbb{E}_{(x_0, x_1) \sim p_0 \times p_1}[\langle \phi(x_0), \phi(x_c) \rangle \mid x_t = x]. \quad (16)$$

Under Assumption 4.2, the gradient of this expectation is equivalent to  $\nabla_x \log Z_t(x; x_c)$ . Substituting this result into the formulation of the reverse SDE from Lemma 4.3 completes the proof.  $\square$

## B.2. Toy Example

We consider a 2D distribution  $p_0(x) = \frac{1}{2}\mathbf{1}[x \in C_1 \cup C_2]$ , where  $C_1 = \{x = (x_1, x_2); -1 \leq x_1 \leq 0, 0 \leq x_2 \leq 1\}$  and  $C_2 = \{x = (x_1, x_2); 0 \leq x_1 \leq 1, -1 \leq x_2 \leq 0\}$ . To learn a velocity field mapping  $p_0$  to the standard normal distribution  $p_1 = \mathcal{N}(0, I)$ , we train a 5-layer MLP with ReLU activation functions following the REPA procedure (Yu et al., 2025). We used Adam (Kingma, 2015) optimizer with learning rate of  $10^{-3}$ , a batch size of 512, and 300 epochs, with a dataset size of 100,000 points. The model utilizes 512-channel intermediate layers, taking a 2D coordinate and time as input to output a 2D velocity vector. We extract representations from the third layer and map them to the alignment target space using a 2-layer MLP projection head.

To mimic the  $\ell_2$  normalization used in REPA, we design a 2D target feature space constrained to the unit circle. Specifically, the target embedding  $\phi(x)$  is defined as:

$$\phi(x) = \left[ \frac{t}{\sqrt{t^2 + (h-w)^2}}, \frac{h-w}{\sqrt{t^2 + (h-w)^2}} \right], \quad (17)$$

where  $t$ ,  $h$ , and  $w$  represent the normalized distances from the cell center, the nearest vertical edge, and the nearest horizontal edge, respectively. The model is trained for 300 epochs using the composite loss  $\mathcal{L}^{\text{diff}} + \beta \mathcal{L}^{\text{align}}$  with  $\beta = 0.5$ .

Figure 7 illustrates 2,000 generated samples (red) alongside the ground-truth distribution (grey). For conditional density sampling, we employ a rejection algorithm (Devroye, 2006) to generate reference points. Diffusion sampling is performed via an Euler-Maruyama solver with 250 steps and an optional guidance scale of  $\lambda = 2$ . The conditional results in the third and fourth columns are induced by target feature vectors  $[-1, 0]$  and  $[0, -1]$ , respectively.



Figure 8. **Impact of representation alignment on SiT’s feature space.** We compare clusters across ImageNet (Deng et al., 2009) using four feature spaces. For each space, we extract features for the entire ImageNet dataset and perform  $k$ -means clustering into 1,000 discrete clusters. Then, we identify the specific cluster associated with a given reference image (indicated by the red frame) and randomly sample other images from that same cluster. Without alignment, the standard SiT model fails to form semantic clusters; features that are close in latent space represent unrelated concepts, which makes these internal representations unsuitable for conditioning. The aligned model successfully mimics the feature space of the visual teacher backbone both before and after the projection layer. This results in semantically consistent clusters. SiT (Align) refers to REPA (Singh et al., 2025) features extracted before the projection layer, whereas SiT (Align + Proj) denotes features extracted after the projection layer.

## C. Complementary Details on Properties of Representation Space (Section 5)

### C.1. Clustering of ImageNet

We perform  $k$ -means clustering across ImageNet (Deng et al., 2009) using  $k = 1000$  clusters across four distinct feature spaces via the FAISS library (Douze et al., 2025). We use the normalized global average of each image’s spatial feature map. Features are extracted from: (i) DINOv2 (Oquab et al., 2024), (ii) SiT-XL/2 with representation alignment (Yu et al., 2025) at the 8th layer (both before and after projection), and (iii) the baseline SiT-XL/2 trained without alignment (Ma et al., 2024) at the same layer. Figure 8 provide two additional cluster comparisons for each feature space.

### C.2. Euclidean Embedding Property

Following (Kadkhodaie et al., 2025), we investigate the Euclidean embedding property. As established in Section 3, there must exist  $0 < A \leq B$  and where the ratio  $B/A$  is reasonably small such that for all  $x_1, x_2$ :

$$A\|\phi(x_1) - \phi(x_2)\|^2 \leq d^2(p_1, p_2) \leq B\|\phi(x_1) - \phi(x_2)\|^2.$$

We now justify the choice of the metric  $d^2$ . Let  $\phi_1$  and  $\phi_2$  be two embeddings that induce the conditional densities  $p_1$  and  $p_2$ , respectively. Under Assumptions 4.1 and 4.2, the tilted distribution is given by:

$$\tilde{p}_0(x; \phi_i) \propto p_0(x) e^{\lambda \mathcal{V}(\phi(x), \phi_i)}. \tag{18}$$

In this experiment, we utilize the full feature map to adhere strictly to our theoretical framework. For this setup, we define  $d^2$  as the symmetric KL divergence:

## Test-Time Conditioning with Representation-Aligned Visual Features

Table 6. **Distribution-level comparison of unconditional REPA-G generations on ImageNet (Deng et al., 2009).** We compare the standard SiT backbone (Ma et al., 2024) (trained without representation alignment) against REPA (Wang et al., 2025) and REPA-E (Leng et al., 2025) variants. All models are trained on ImageNet. For each method block, the first row denotes metrics for unconditional generation, serving as a baseline for the REPA-G results.  $\mathbf{F}_{\text{SiT}}^*$  denotes features extracted after the projection layer in REPA-based models. Gray results are from Table 1 in the main text for ease of comparison.

Model	Cond.	Full Feature Map					Masked Feature Map					Average Feature Map				
		FID↓	sFID↓	IS↑	Prec.↑	Rec.↑	FID↓	sFID↓	IS↑	Prec.↑	Rec.↑	FID↓	sFID↓	IS↑	Prec.↑	Rec.↑
SiT	-	45.02	9.02	22.33	0.50	0.63	45.02	9.02	22.33	0.50	0.63	45.02	9.02	22.33	0.50	0.63
	$\mathbf{F}_{\text{SiT}}^*$	71.35	72.08	14.73	0.33	0.54	51.88	42.36	15.76	0.27	0.52	65.99	22.52	16.69	0.36	0.52
REPA	-	26.58	6.85	41.31	0.56	<b>0.70</b>	26.58	6.85	41.31	0.56	<b>0.70</b>	26.58	6.85	41.31	0.56	<b>0.70</b>
	$\mathbf{F}_{\text{DINO}}$	7.23	8.86	199.69	0.65	0.69	14.17	10.59	135.08	0.58	0.64	29.06	16.79	83.85	0.46	0.69
	$\mathbf{F}_{\text{SiT}}^*$	<b>2.09</b>	<b>6.17</b>	<b>260.97</b>	<b>0.74</b>	<b>0.70</b>	<b>2.67</b>	<b>4.86</b>	<b>222.71</b>	<b>0.74</b>	0.69	<b>6.26</b>	<b>6.14</b>	<b>159.14</b>	<b>0.68</b>	<b>0.70</b>
	$\mathbf{F}_{\text{SiT}}^*$	<b>6.65</b>	<b>7.59</b>	<b>186.60</b>	<b>0.66</b>	<b>0.70</b>	<b>12.29</b>	<b>9.72</b>	<b>135.77</b>	<b>0.61</b>	<b>0.65</b>	<b>22.10</b>	<b>13.86</b>	<b>92.34</b>	<b>0.54</b>	<b>0.66</b>
REPA-E	-	15.07	4.46	55.14	0.65	<b>0.69</b>	15.07	4.46	55.14	0.65	<b>0.69</b>	15.07	<b>4.46</b>	55.14	0.65	<b>0.69</b>
	$\mathbf{F}_{\text{DINO}}$	<b>1.45</b>	<b>4.07</b>	<b>264.69</b>	<b>0.76</b>	<b>0.69</b>	2.30	4.84	212.25	0.75	0.67	3.24	5.20	188.92	0.73	0.67
	$\mathbf{F}_{\text{SiT}}^*$	2.15	6.64	264.48	0.75	0.68	<b>1.79</b>	<b>4.13</b>	<b>237.37</b>	<b>0.76</b>	0.68	<b>2.50</b>	4.81	<b>201.13</b>	<b>0.74</b>	<b>0.69</b>
	$\mathbf{F}_{\text{SiT}}^*$	<b>1.42</b>	4.10	<b>257.23</b>	<b>0.76</b>	<b>0.70</b>	2.01	4.73	216.19	0.76	0.67	2.65	5.05	191.79	<b>0.76</b>	0.65

$$d^2(p_1, p_2) := \text{KL}(p_1 \| p_2) + \text{KL}(p_2 \| p_1) \quad (19)$$

$$= \mathbb{E}_{p_1} \left[ \log \frac{p_1}{p_2} \right] + \mathbb{E}_{p_2} \left[ \log \frac{p_2}{p_1} \right] \quad (20)$$

$$= \frac{\lambda}{N} \sum_{n=1}^N \left( \mathbb{E}_{p_1} [\langle [\phi(x)]_n, [\phi_1 - \phi_2]_n \rangle] + \mathbb{E}_{p_2} [\langle [\phi(x)]_n, [\phi_2 - \phi_1]_n \rangle] \right) \quad (21)$$

$$= \frac{\lambda}{N} \sum_{n=1}^N \langle [\mathbb{E}_{p_1} [\phi(x)] - \mathbb{E}_{p_2} [\phi(x)]]_n, [\phi_1 - \phi_2]_n \rangle. \quad (22)$$

## D. Complementary Details on Design of Potential $\mathcal{V}$ (Section 6)

### D.1. Selective Patch Alignment (SPA)

We define the Selective Patch Alignment (SPA) potential as:

$$\mathcal{V}^{\text{SPA}}(h, h^*) = T \log \left[ \sum_{n=1}^N \exp \left( \frac{\langle [h]_n, [h^*]_i \rangle}{T} \right) \right]. \quad (23)$$

As discussed in Section 6.2, the temperature parameter  $T$  modulates the sparsity of this selection. In the limit  $T \rightarrow 0$ , the potential is dominated by the patch most similar to  $h_i^*$ , effectively performing a "hard" selection. Conversely, as  $T \rightarrow \infty$ , the patches are weighted equally, recovering the global averaging behavior of IPA. Consequently, SPA can be viewed as a generalization of IPA, where  $T$  serves as a tunable parameter to optimize spatial correspondence. This relationship is further elucidated by the gradient:

$$\nabla_{h_k} \mathcal{V}^{\text{SPA}}(h, h^*) = N \sigma \left[ \frac{1}{T} (\langle h_n, h_i^* \rangle)_{n \in [1, N]} \right]_k \nabla_{h_k} \mathcal{V}^{\text{IPA}}(h, h^*), \quad (24)$$

where  $\sigma(\cdot)$  denotes the softmax function. Here, the gradient of SPA is simply a reweighted version of the IPA gradient, where the weights are determined by the relative similarity of each patch to the target feature.

## E. More Experimental Results (Section 7)

**Hyperparameters.** For single-source experiments, we set  $\lambda = 50,000$  based on a coarse grid search over the full dataset. For multi-source guidance experiments, hyperparameters  $\lambda$  and temperature  $T$  are set to 10,000 and 0.1, respectively, based on a grid search over a diverse 5-class ImageNet subset (i.e., *goldfish*, *shark*, *golden retriever*, *bald eagle*, *tiger*). For each class, 10 random samples are combined with 8 hand-selected target background features.

Table 7. Instance-level comparison of unconditional REPA-G generations on ImageNet (Deng et al., 2009). Setup is the same as in Table 1. Alignment is measured with DINOv2 (Oquab et al., 2024), JEPA (Assran et al., 2023), CLIP (Radford et al., 2021), MAE (He et al., 2022) and MoCov3 (Chen et al., 2021) feature spaces, supplemented by PSNR for pixel-level fidelity.  $\mathbf{F}_{\text{SIT}}^*$  denotes features extracted after the projection layer in REPA-based models. Gray results are from Table 1 in the main text for ease of comparison.

Model	Feat.	Full Feature Map						Masked Feature Map						Average Feature Map					
		DINOv2	JEPA	CLIP	MAE	MoCo	PSNR	DINOv2	JEPA	CLIP	MAE	MoCo	PSNR	DINOv2	JEPA	CLIP	MAE	MoCo	PSNR
SiT	$\mathbf{F}_{\text{SIT}}$	0.27	0.36	0.43	<b>0.93</b>	<b>0.78</b>	15.35	0.44	0.48	0.46	<b>0.95</b>	<b>0.82</b>	17.98	0.12	0.35	0.83	<b>0.99</b>	<b>0.95</b>	7.74
REPA	$\mathbf{F}_{\text{DINO}}$	0.75	0.61	0.58	0.94	0.86	11.02	0.77	0.60	0.57	0.94	0.84	10.63	0.76	0.69	0.92	0.99	0.98	8.00
	$\mathbf{F}_{\text{SIT}}$	0.85	0.78	0.71	<b>0.98</b>	<b>0.95</b>	20.46	0.87	0.79	0.71	<b>0.98</b>	<b>0.94</b>	20.72	0.84	0.84	0.95	<b>0.99</b>	<b>0.990</b>	10.82
	$\mathbf{F}_{\text{SIT}}^*$	0.72	0.63	0.59	0.94	0.87	11.32	0.74	0.63	0.58	0.94	0.86	11.02	0.77	0.72	0.92	0.99	0.98	8.01
REPA-E	$\mathbf{F}_{\text{DINO}}$	0.83	0.69	0.64	0.96	0.90	15.23	0.85	0.68	0.63	0.95	0.88	14.36	0.91	0.83	0.96	0.99	0.99	10.97
	$\mathbf{F}_{\text{SIT}}$	0.86	0.76	0.71	<b>0.97</b>	<b>0.94</b>	18.68	0.89	0.78	0.71	<b>0.98</b>	<b>0.94</b>	19.07	0.91	0.88	0.96	<b>0.99</b>	<b>0.99</b>	11.96
	$\mathbf{F}_{\text{SIT}}^*$	0.81	0.70	0.65	0.96	0.91	15.91	0.83	0.71	0.65	0.96	0.90	15.13	0.90	0.86	0.96	0.99	0.99	11.12

Table 8. Zero-shot evaluation on COCO (Lin et al., 2014) dataset using instance-level metrics. Alignment is measured with DINOv2 (Oquab et al., 2024), JEPA (Assran et al., 2023), CLIP (Radford et al., 2021), MAE (He et al., 2022) and MoCov3 (Chen et al., 2021) feature spaces, supplemented by PSNR for pixel-level fidelity.  $\mathbf{F}_{\text{SIT}}^*$  denotes features extracted after the projection layer in REPA-based models.

Model	Cond.	Full Feature Map						Masked Feature Map						Average Feature Map					
		DINOv2	JEPA	CLIP	MAE	MoCo	PSNR	DINOv2	JEPA	CLIP	MAE	MoCo	PSNR	DINOv2	JEPA	CLIP	MAE	MoCo	PSNR
SiT	$\mathbf{F}_{\text{SIT}}$	<b>0.25</b>	<b>0.35</b>	<b>0.4</b>	<b>0.93</b>	<b>0.76</b>	<b>15.18</b>	<b>0.4</b>	<b>0.45</b>	<b>0.44</b>	<b>0.95</b>	<b>0.82</b>	<b>18.56</b>	<b>0.11</b>	<b>0.38</b>	<b>0.81</b>	<b>0.99</b>	<b>0.95</b>	<b>7.66</b>
REPA	$\mathbf{F}_{\text{DINO}}$	0.74	0.60	0.56	0.94	0.85	10.72	0.75	0.56	0.55	0.93	0.84	10.85	0.74	0.68	0.90	0.99	0.98	7.72
	$\mathbf{F}_{\text{SIT}}$	<b>0.84</b>	<b>0.78</b>	<b>0.7</b>	<b>0.98</b>	<b>0.95</b>	<b>20.61</b>	<b>0.84</b>	<b>0.76</b>	<b>0.69</b>	<b>0.98</b>	<b>0.94</b>	<b>21.38</b>	<b>0.8</b>	<b>0.82</b>	<b>0.92</b>	<b>0.99</b>	<b>0.99</b>	<b>10.47</b>
	$\mathbf{F}_{\text{SIT}}^*$	0.70	0.63	0.56	0.94	0.87	11.01	0.71	0.59	0.56	0.94	0.86	11.28	0.73	0.70	0.90	0.99	0.98	7.73
REPA-E	$\mathbf{F}_{\text{DINO}}$	0.82	0.68	0.63	0.95	0.89	14.78	0.84	0.64	0.62	0.95	0.88	14.72	<b>0.9</b>	0.82	0.94	1.00	0.99	10.66
	$\mathbf{F}_{\text{SIT}}$	<b>0.84</b>	<b>0.76</b>	<b>0.7</b>	<b>0.97</b>	<b>0.94</b>	<b>18.58</b>	<b>0.86</b>	<b>0.75</b>	<b>0.69</b>	<b>0.98</b>	<b>0.94</b>	<b>19.67</b>	0.89	<b>0.86</b>	<b>0.95</b>	<b>0.99</b>	<b>0.99</b>	<b>11.63</b>
	$\mathbf{F}_{\text{SIT}}^*$	0.79	0.70	0.63	0.95	0.91	15.57	0.81	0.67	0.63	0.95	0.90	15.62	0.88	0.84	0.94	1.00	0.99	10.89

### E.1. More Results on Unconditional Generation

As detailed in Section 7, we also evaluated features extracted after the projection layer for REPA-based models, but observed no significant performance difference. These results, provided in Table 6, complement those in Table 1.

We further complement Table 2 by providing alignment scores within the MAE (He et al., 2022) and MoCov3 (Chen et al., 2021) feature spaces. As shown in Table 7, these scores remain consistent with the trends observed across other feature representations. Similarly, we report alignment scores for the COCO dataset (Lin et al., 2014) in Table 8.

### E.2. Results on Conditional Generation

Analogous to our unconditional experiments, we evaluate conditional generation by providing the class index alongside the noisy latent as input. Results for this setup are reported in Table 9 for distribution-level metrics and Table 10 for instance-level alignment.

### E.3. Runtime Evaluation

We measured throughput on a single H100 GPU with a batch size of 256, averaging across 20 batches after a 5-batch warmup. As reported in Table 11, backpropagating gradients through the first 8-transformer blocks naturally increases latency; however, the resulting inference speeds remain well within an acceptable range.

### E.4. Complementary Details on Multiple-Source Compositional Generation

**More Details on Classes.** In Table 12, we provide the list of 50 ImageNet (Deng et al., 2009) classes and 8 hand-selected target backgrounds used to evaluate multi-source compositional generation.

**Patch Metrics for Multi-Concept.** As detailed in Section 7, we evaluate the quality of our compositions using patch-wise metrics. For each patch  $n$  in the generated feature map  $h_{\text{gen}}$ , we calculate the cosine similarity against both the corresponding anchor patch  $[h_{\text{ref}}]_n$  and the broadcasted target feature  $[\tilde{h}_{\text{target}}]_n$ :

$$s_{\text{anchor},n} = \cos([h_{\text{gen}}]_n, [h_{\text{ref}}]_n), \quad s_{\text{target},n} = \cos([h_{\text{gen}}]_n, [\tilde{h}_{\text{target}}]_n) \quad (25)$$

## Test-Time Conditioning with Representation-Aligned Visual Features

Table 9. **Distribution-level comparison of class-conditional REPA-G generations on ImageNet (Deng et al., 2009).** We compare the standard SiT backbone (Ma et al., 2024) (trained without representation alignment) against REPA (Wang et al., 2025) and REPA-E (Leng et al., 2025) variants. All models are trained on ImageNet. For each method block, the first row denotes metrics for unconditional generation, serving as a baseline for the REPA-G results.  $F_{\text{SiT}}^*$  denotes features extracted after the projection layer in REPA-based models.

Model	Cond.	Full Feature Map					Masked Feature Map					Average Feature Map				
		FID↓	sFID↓	IS↑	Prec.↑	Rec.↑	FID↓	sFID↓	IS↑	Prec.↑	Rec.↑	FID↓	sFID↓	IS↑	Prec.↑	Rec.↑
SiT	-	<b>10.17</b>	<b>8.53</b>	<b>124.93</b>	<b>0.67</b>	<b>0.67</b>	<b>10.17</b>	<b>8.53</b>	<b>124.93</b>	<b>0.67</b>	<b>0.67</b>	<b>10.17</b>	<b>8.53</b>	<b>124.93</b>	<b>0.67</b>	<b>0.67</b>
	$F_{\text{SiT}}$	71.05	49.21	17.42	0.29	0.58	62.65	13.98	19.82	0.34	0.65	130.14	53.16	2.08	0.50	0.04
REPA	-	5.92	<b>5.92</b>	157.10	0.70	<b>0.68</b>	5.92	5.92	157.10	0.70	<b>0.68</b>	<b>5.92</b>	<b>5.92</b>	<b>157.10</b>	<b>0.70</b>	<b>0.68</b>
	$F_{\text{DINO}}$	6.24	8.43	197.64	0.69	0.64	13.68	10.21	127.72	0.61	0.60	27.94	15.32	84.04	0.49	0.66
	$F_{\text{SiT}}$	<b>2.14</b>	6.71	<b>254.99</b>	<b>0.77</b>	0.65	<b>3.34</b>	<b>5.68</b>	<b>199.55</b>	<b>0.77</b>	0.63	11.24	8.59	122.54	0.63	0.67
	$F_{\text{SiT}}^*$	5.60	7.14	186.45	0.71	0.64	11.77	9.41	131.34	0.64	0.60	21.98	13.61	91.11	0.56	0.62
REPA-E	-	1.71	4.19	220.60	0.77	0.66	<b>1.71</b>	<b>4.19</b>	220.60	0.77	<b>0.66</b>	<b>1.71</b>	<b>4.19</b>	<b>220.60</b>	<b>0.77</b>	0.66
	$F_{\text{DINO}}$	1.53	4.10	266.85	0.78	0.66	3.46	5.03	188.62	0.74	0.65	8.07	7.41	160.08	0.66	<b>0.69</b>
	$F_{\text{SiT}}$	1.97	6.67	<b>269.26</b>	0.78	0.66	1.98	4.24	<b>223.53</b>	<b>0.77</b>	0.65	3.23	5.39	192.17	0.72	0.67
	$F_{\text{SiT}}^*$	<b>1.53</b>	<b>4.04</b>	257.50	<b>0.78</b>	<b>0.66</b>	2.85	4.76	193.55	0.75	0.65	6.12	7.37	165.95	0.70	0.66

Next, patches are assigned to the partition ( $\Omega_{\text{anchor}}$  or  $\Omega_{\text{target}}$ ) where they exhibit the highest similarity.

$$n \in \begin{cases} \Omega_{\text{anchor}} & \text{if } s_{\text{anchor},n} > s_{\text{target},n} \\ \Omega_{\text{target}} & \text{otherwise} \end{cases} \quad (26)$$

The resulting scores,  $\mathcal{S}_{\text{anchor}}$  and  $\mathcal{S}_{\text{target}}$ , are the average alignments within their respective partitions:

$$\mathcal{S}_{\text{anchor}} = \frac{1}{|\Omega_{\text{anchor}}|} \sum_{n \in \Omega_{\text{anchor}}} s_{\text{anchor},n} \quad (27)$$

$$\mathcal{S}_{\text{target}} = \frac{1}{|\Omega_{\text{target}}|} \sum_{n \in \Omega_{\text{target}}} s_{\text{target},n} \quad (28)$$

Finally, we compute a combined score by taking the arithmetic mean of  $\mathcal{S}_{\text{anchor}}$  and  $\mathcal{S}_{\text{target}}$ :

$$\mathcal{S}_{\text{combined}} = \frac{1}{2} (\mathcal{S}_{\text{target}} + \mathcal{S}_{\text{anchor}}) \quad (29)$$

These metrics capture the model’s precision in structural preservation alongside its responsiveness to the target potential  $\mathcal{V}$ .

### E.5. More Qualitative Results

Figure 9 and 10 provides additional qualitative results on ImageNet (Deng et al., 2009) and COCO (Lin et al., 2014) using our best configuration: a class-conditioned model guided by features extracted after the REPA-E (Singh et al., 2025) projection layer.

Table 10. **Distribution-level comparison of class-conditional REPA-G generations on ImageNet (Deng et al., 2009).** We compare the standard SiT backbone (Ma et al., 2024) (trained without representation alignment) against REPA (Wang et al., 2025) and REPA-E (Leng et al., 2025) variants. All models are trained on ImageNet. For each method block, the first row denotes metrics for unconditional generation, serving as a baseline for the REPA-G results.  $F_{\text{SiT}}^*$  denotes features extracted after the projection layer in REPA-based models.

Model	Cond.	Full Feature Map						Masked Feature Map						Average Feature Map					
		DINO	JEPA	CLIP	MAE	MoCo	PSNR	DINO	JEPA	CLIP	MAE	MoCo	PSNR	DINO	JEPA	CLIP	MAE	MoCo	PSNR
SiT	$F_{\text{SiT}}$	<b>0.3</b>	<b>0.39</b>	<b>0.43</b>	<b>0.94</b>	<b>0.78</b>	<b>14.79</b>	<b>0.4</b>	<b>0.44</b>	<b>0.44</b>	<b>0.95</b>	<b>0.81</b>	<b>17.66</b>	<b>0.13</b>	<b>0.37</b>	<b>0.83</b>	<b>0.99</b>	<b>0.95</b>	<b>8.64</b>
REPA	$F_{\text{DINO}}$	0.74	0.59	0.57	0.94	0.85	10.47	0.76	0.58	0.56	0.93	0.83	10.30	0.75	0.68	0.92	<b>0.99</b>	0.98	8.05
	$F_{\text{SiT}}$	<b>0.84</b>	<b>0.77</b>	<b>0.7</b>	<b>0.98</b>	<b>0.94</b>	<b>19.6</b>	<b>0.86</b>	<b>0.77</b>	<b>0.7</b>	<b>0.98</b>	<b>0.94</b>	<b>20</b>	<b>0.79</b>	<b>0.8</b>	<b>0.93</b>	<b>0.99</b>	<b>0.99</b>	<b>10.36</b>
	$F_{\text{SiT}}^*$	0.71	0.61	0.58	0.94	0.86	10.71	0.73	0.61	0.57	0.94	0.85	10.60	0.76	0.70	0.92	<b>0.99</b>	0.98	8.02
REPA-E	$F_{\text{DINO}}$	0.82	0.68	0.63	0.95	0.89	14.79	0.84	0.66	0.62	0.95	0.87	13.84	0.88	0.79	0.95	<b>0.99</b>	0.99	10.34
	$F_{\text{SiT}}$	<b>0.85</b>	<b>0.76</b>	<b>0.7</b>	<b>0.97</b>	<b>0.94</b>	<b>18.57</b>	<b>0.87</b>	<b>0.77</b>	<b>0.7</b>	<b>0.97</b>	<b>0.93</b>	<b>18.81</b>	<b>0.89</b>	<b>0.85</b>	<b>0.96</b>	<b>0.99</b>	<b>0.99</b>	<b>11.58</b>
	$F_{\text{SiT}}^*$	0.80	0.69	0.64	0.96	0.90	15.33	0.82	0.68	0.63	0.95	0.89	14.41	0.88	0.80	0.95	<b>0.99</b>	0.99	10.45

Table 11. **Inference throughput.** Feature conditioning requires backpropagating gradients through the initial blocks of the transformer. While this results in a slight reduction in throughput, the computational overhead remains minimal. The baseline is the standard class-conditioned REPA-E model (Leng et al., 2025), whereas our approach incorporates feature guidance into this framework.

Runtime	Throughput (Images per Second) ↑
Baseline	0.53
REPA-G w/ feature conditioning (ours)	0.39

Table 12. A diverse set of 50 ImageNet (Deng et al., 2009) classes and 8 hand-selected target backgrounds used to evaluate multi-source compositional generation.

Super-category	Fine-grained Class Names
Animals	Golden retriever, Tabby cat, Zebra, Bullfrog, Tarantula, Goldfish, Monarch butterfly, Crane, Bald eagle, Tiger
Movables	Bicycle, Motor scooter, Mountain bike, Baby stroller, Lawnmower, Shopping cart, Tricycle, Car wheel, Fire engine, Sports car
Food Flora	Strawberry, Banana, Granny Smith, Plate, Pizza, Cheeseburger, Agaric, Acorn, Burrito, Bee
Tools Tech	Acoustic guitar, Broom, Hammer, Screwdriver, Soccer ball, Tennis racket, Crash helmet, Wall clock, Laptop, Ping-pong ball
Household	Teapot, Coffeepot, Toaster, Vase, Cowboy hat, Running shoe, Backpack, Umbrella, Teddy bear, Balloon
<i>Our hand-selected target backgrounds</i>	
Background	Grass, Dirt, Snow, Ice, Carpet, Water, Brick, Wood

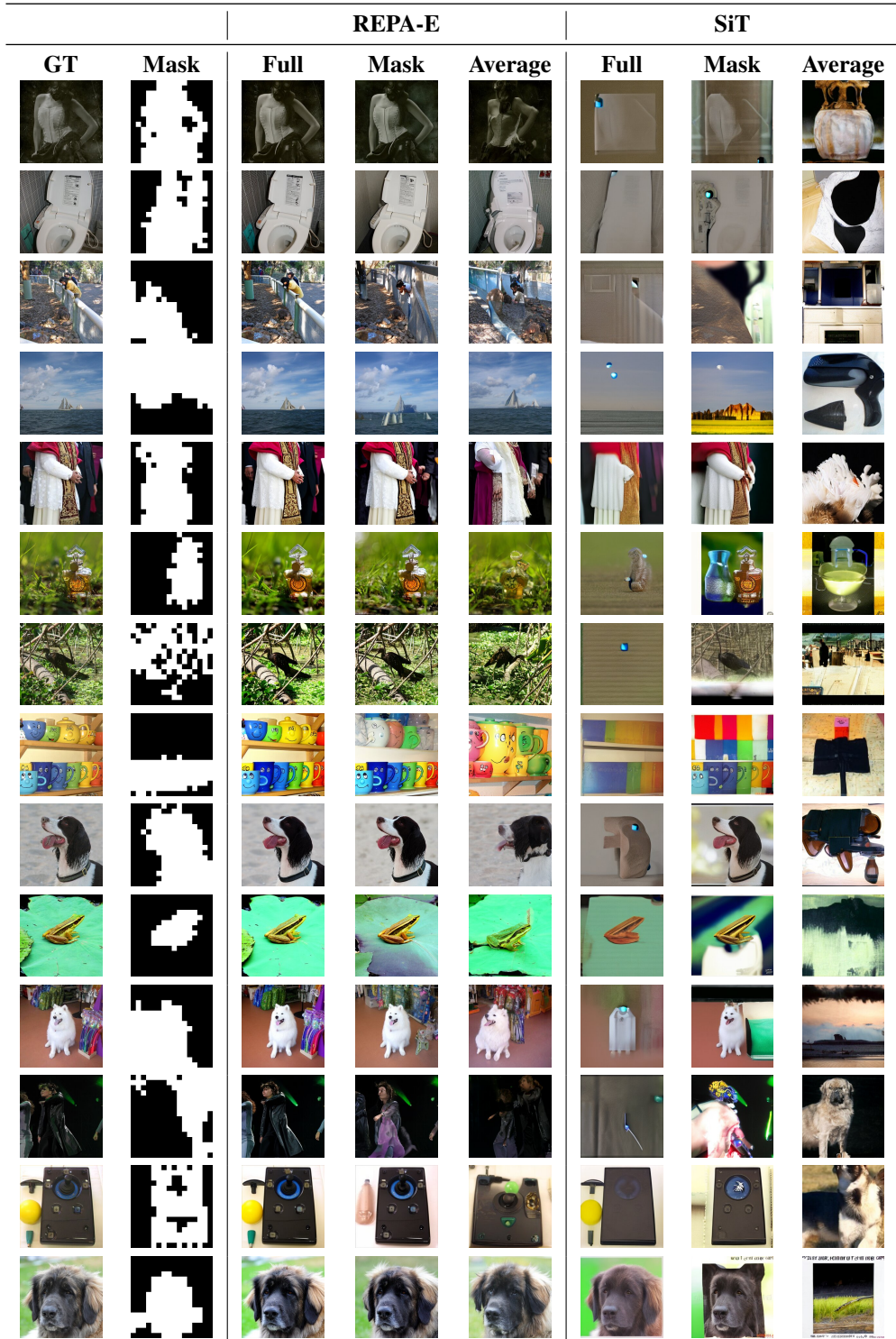


Figure 9. Qualitative results on ImageNet dataset (Deng et al., 2009). We present randomly selected samples from various conditioning modes. The first row shows the ground-truth (anchor) images, followed by their unsupervised foreground masks. Subsequent rows show generations using the full feature map, the masked feature map (using the corresponding mask), and the averaged feature map. All visualizations are from our best configuration: a class-conditioned model guided by features from the REPA-E (Leng et al., 2025) after projection layer. The following block displays the corresponding results for standard SiT (Ma et al., 2024) model trained without representation alignment. We observe that SiT models trained without representation alignment struggle to produce coherent results under feature guidance.

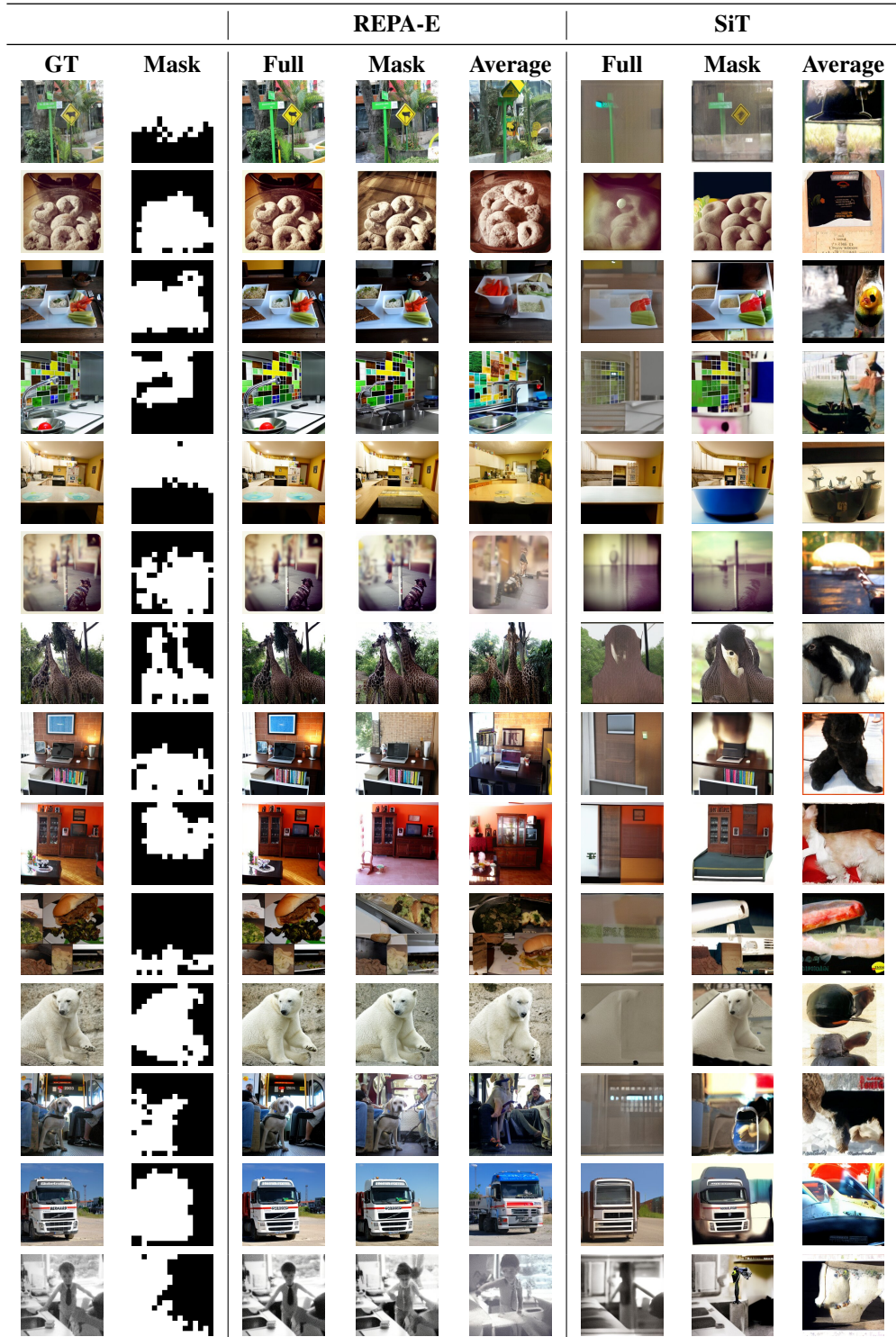


Figure 10. Qualitative results on COCO dataset (Lin et al., 2014). We present randomly selected samples from various conditioning modes. The first row shows the ground-truth (anchor) images, followed by their unsupervised foreground masks. Subsequent rows show generations using the full feature map, the masked feature map (using the corresponding mask), and the averaged feature map. All visualizations are from our best configuration: a class-conditioned model guided by features from the REPA-E (Leng et al., 2025) after projection layer. The following block displays the corresponding results for standard SiT (Ma et al., 2024) model trained without representation alignment. We observe that SiT models trained without representation alignment struggle to produce coherent results under feature guidance.